

Co₃O₄ hollow nanoparticles embedded in mesoporous walls of carbon nanoboxes for efficient lithium storage

Huang, Yi; Fang, Yongjin; Lu, Xue Feng; Luan, Deyan; Lou, David Xiong Wen

2020

Huang, Y., Fang, Y., Lu, X. F., Luan, D. & Lou, D. X. W. (2020). Co₃O₄ hollow nanoparticles embedded in mesoporous walls of carbon nanoboxes for efficient lithium storage. *Angewandte Chemie International Edition*, 59(45), 19914-19918.
<https://dx.doi.org/10.1002/anie.202008987>

<https://hdl.handle.net/10356/147392>

<https://doi.org/10.1002/anie.202008987>

This is the peer reviewed version of the following article: Huang, Y., Fang, Y., Lu, X. F., Luan, D. & Lou, D. X. W. (2020). Co₃O₄ hollow nanoparticles embedded in mesoporous walls of carbon nanoboxes for efficient lithium storage. *Angewandte Chemie International Edition*, 59(45), 19914-19918. <https://dx.doi.org/10.1002/anie.202008987>, which has been published in final form at <https://doi.org/10.1002/anie.202008987>. This article may be used for non-commercial purposes in accordance with Wiley Terms and Conditions for Use of Self-Archived Versions.

Downloaded on 05 Apr 2024 15:30:35 SGT

Co₃O₄ Hollow Nanoparticles Embedded in Mesoporous Walls of Carbon Nanoboxes for Efficient Lithium Storage

Yi Huang, Yongjin Fang, Xue Feng Lu, Deyan Luan,* and Xiong Wen (David) Lou*

[*] Dr. Y. Huang, Dr. Y. J. Fang, Dr. X. F. Lu, Dr. D. Y. Luan, Prof. X. W. Lou

School of Chemical and Biomedical Engineering, Nanyang Technological University, 62 Nanyang Drive, Singapore, 637459, Singapore

Email: dyluan@ntu.edu.sg; xwlou@ntu.edu.sg; davidlou88@gmail.com

Webpage: <http://www.ntu.edu.sg/home/xwlou/>

Abstract

Confining nanostructured electrode materials in porous carbon represents an effective strategy for improving the electrochemical performance of lithium-ion batteries. Herein, we report the elaborate design and synthesis of hybrid hollow nanostructures composed of highly dispersed Co₃O₄ hollow nanoparticles (sub-20 nm) embedded in the mesoporous walls of carbon nanoboxes (denoted as H-Co₃O₄@MCNBs) as an anode material for lithium-ion batteries. The facile metal-organic framework (MOF)-engaged strategy for the synthesis of H-Co₃O₄@MCNBs involves chemical etching-coordination and subsequent two-step annealing treatments. Owing to the unique structural merits including more active interfacial sites, effectively alleviated volume variation, good and stable electrical contact, and easy access of Li⁺ ions, the obtained H-Co₃O₄@MCNBs exhibit excellent lithium storage performance in terms of high specific capacity, excellent rate capability and cycling stability.

Keywords: hollow structures, metal-organic frameworks, cobalt oxides, lithium-ion batteries.

To meet the increasing demand of high-performance batteries for a wide range applications from portable electronic devices to electric vehicles and grids, substantial efforts have been devoted to searching for alternative anode materials with higher capacity and better rate capability for lithium-ion batteries (LIBs).^[1-3] Transition metal oxides (TMOs) are promising candidates for LIBs due to their low cost, environment friendliness, and higher theoretical capacity relative to the traditional graphite electrode.^[4] Among them, cobalt oxide (Co_3O_4), which can theoretically deliver as high as three times the capacity of graphite due to its eight-electron transfer reaction upon cycling,^[5,6] has been intensively studied as attractive anode materials.^[7-13] However, its practical applications are largely hampered by the huge volumetric expansion, severe particle aggregation during lithiation/delithiation processes, and sluggish ion/electron transfer, which lead to low capacity and poor cycling stability.^[4]

Recently, the confinement of nanostructured electroactive materials into hollow porous carbon nanostructures has emerged as an effective strategy for addressing the above issues.^[14-16] The conductive carbon shell can not only improve the mechanical flexibility of hybrid materials and buffer their volume changes, but also restrict the aggregation of nanostructured electroactive materials during the charge/discharge processes,^[15] thus leading to the improved cycling stability for lithium storage. Moreover, the design of hollow nanostructured TMOs with highly exposed surface area and active sites is considered as an efficient approach to enhance electrochemical performance for LIBs.^[11,17] The presence of interior voids not only provides sufficient space to accommodate volume changes during lithiation/delithiation processes but also shortens the Li^+ ion diffusion distance.^[7] Especially, the hollow nanomaterials with ultrafine (< 20 nm) and highly dispersed features can further enlarge surface area and expose more active sites, resulting in higher specific capacity and faster reaction kinetics.^[18] Therefore, the integration of above structural advantages to rationally design and construct ultrafine TMOs hollow nanoparticles (NPs) well confined in hollow porous carbon matrix is highly attractive for high-

performance LIBs, but still remains as a challenging task to date. Currently, metal-organic frameworks (MOFs) have been demonstrated as effective precursors or templates for the synthesis of TMOs/porous carbon nanocomposites via thermal treatment under a controlled atmosphere.^[9,19,20] Despite the progress, the facile construction of MOF-derived hybrid hollow architectures composed of hollow TMOs embedded homogeneously in the porous carbon matrix is still challenging because of the limitations of synthetic strategies.

Herein, we demonstrate a facile MOF-engaged etching-pyrolysis-oxidation strategy for the design and fabrication of an elegant hybrid structure consisting of highly dispersed ultrafine Co_3O_4 hollow NPs embedded in mesoporous walls of carbon nanoboxes (denoted as $\text{H-Co}_3\text{O}_4@\text{MCNBs}$). This elegant hybrid structure integrates the remarkable structural advantages of the different functional subunits. To be specific, the ultrafine Co_3O_4 hollow NPs can expose more active interfacial sites, greatly promote the diffusion of Li^+ ions, and effectively alleviate the volume variation during the electrochemical reactions. Encapsulating Co_3O_4 NPs with high dispersion in MCNBs offers good and stable electrical contact between the Co_3O_4 and the relatively conductive carbon, ensures fast Li^+ ion migration, and prevents the aggregation of Co_3O_4 NPs during the cycling processes. As a result, when evaluated as the anode material in LIBs, the obtained $\text{H-Co}_3\text{O}_4@\text{MCNBs}$ exhibited excellent lithium storage capacity, rate capability, and cycling stability.

The synthesis procedure of the $\text{H-Co}_3\text{O}_4@\text{MCNBs}$ involves the following steps as illustrated in **Figure 1**. Initially, uniform Co-based zeolitic imidazolate framework (ZIF-67) nanocubes (NCs) as the templating precursor are synthesized through a modified surfactant-assisted approach.^[21] Next, the ZIF-67 NCs are etched by tannic acid (TA) to form the TA-Co network nanoboxes (NBs) through a controlled chemical etching-coordination process. More specifically, the chemical etching by the released protons from TA^[22-24] generates the hollow structure and simultaneously transforms the composition through

coordination of TA and Co^{2+} released from ZIF-67 to the TA-Co network shell because of the strong chelating capability between TA and metal ions (Figure S1, see Supporting Information).^[25-27] After the pyrolysis treatment in flowing N_2 atmosphere, these TA-Co NBs are transformed to solid Co NPs confined in the walls of MCNBs (denoted as Co@MCNBs). During this step, the TA is pyrolyzed to form carbon, which serves as a reducing agent to reduce Co^{2+} into metallic Co NPs. Lastly, the Co NPs are oxidized to Co_3O_4 hollow NPs via thermal annealing in air while the MCNBs can be well retained, producing H- Co_3O_4 @MCNBs.

The typical field-emission scanning electron microscopy (FESEM) images, transmission electron microscopy (TEM) image and X-ray diffraction (XRD) pattern show the successful synthesis of ZIF-67 NCs with the well-defined cubic morphology, uniform size distribution, smooth surface, and solid nature (Figure S2). After the chemical etching and coordination reaction in TA solution (1 mg mL^{-1}), FESEM images of the obtained TA-Co NBs show that the uniform cubic morphology can be well preserved and the surface remains smooth (**Figure 2a, b**). The hollow interior can be obviously observed from the TEM images (Figure 2c and Figure S3). As revealed by the XRD pattern, the TA-Co NBs are amorphous and the diffraction peaks attributed to the ZIF-67 precursor completely disappear (Figure S4), indicating the completion of the chemical transformation. The surface chemical composition and elemental state of the TA-Co NBs were investigated by X-ray photoelectron spectroscopy (XPS) measurements (Figure S5a). The peaks in high-resolution spectrum of C 1s are attributed to C=O, C-O and C-C (Figure S5b), which are present in the structure of TA (Figure S1),^[27] and the Co ions in the TA-Co NBs are predominantly divalent Co^{2+} observed from the high-resolution spectrum of Co 2p (Figure S5c). The Fourier transform infrared (FTIR) spectrum of TA-Co NBs displays that the main peaks are attributed to the stretching vibration of functional groups from TA (Figure S6), indicating the complete substitution of 2-methylimidazole by TA after etching. These results suggest that the TA-Co NBs have been successfully

synthesized through the TA etching accompanied by the coordination reaction between TA and Co^{2+} (Figure S7).^[23,28-30] After being annealed in a N_2 atmosphere, the TA-Co NBs can be converted to Co@MCNBs. The formation of metallic Co is confirmed by the XRD pattern, and the characteristic D band (1328 cm^{-1}) and G band (1580 cm^{-1}) peaks of carbon can be observed in the Raman spectrum of Co@MCNBs (Figure S8).^[31] The FESEM images display that the cubic shape is preserved (Figure 2d and Figure S9). Further TEM observations show that the highly uniform and discrete Co NPs with an average size of about 12 nm are embedded in the wall of carbon NBs (Figures 2e, f and Figure S9). The clear lattice fringes with an interplanar distance of 0.20 nm measured from high-resolution TEM (HRTEM) image can be ascribed to the (111) planes of the metallic Co (Figure 2g). High-angle annular dark-field scanning transmission electron microscopy (HAADF-STEM) images clearly show that the solid NPs are highly dispersed and embedded in the carbon wall (Figure 2h, i), and the associated elemental mapping images show that the C and Co elements are distributed uniformly in the nanobox (Figure 2j-l). In addition, the existence of mesopores in the wall of carbon NBs is revealed by the type-IV adsorption-desorption isotherm curves with an obvious hysteresis loop (Figure S10).

After subsequent low-temperature oxidation in air at 200°C , the Co@MCNBs are converted to $\text{H-Co}_3\text{O}_4$ @MCNBs. The XRD diffraction peaks of $\text{H-Co}_3\text{O}_4$ @MCNBs can be perfectly indexed to cubic Co_3O_4 , and the Raman spectrum displays that the characteristic D and G band peaks of carbon are maintained and two peaks attributed to Co_3O_4 appear after the oxidation process (Figure S11). FESEM images show that the nanobox morphology is well maintained (**Figure 3a** and Figure S12). Observed from TEM images (Figure 3b, c), the hollow NPs with an average size of ~ 16 nm are well confined in the carbon wall of NBs and still exhibit high dispersion. The formation of Co_3O_4 hollow NPs from Co solid NPs is commonly attributed to the nanoscale Kirkendall effect during the annealing process.^[8,11,32-34] The HRTEM image shows the interplanar distance of about 0.24 nm, ascribed to the (311) planes of

the cubic Co_3O_4 (Figure 3d). As shown in the HAADF-STEM images (Figure 3e-g) and associated elemental mapping images (Figure 3h-k), the hollow structure of Co_3O_4 NPs confined in the carbon wall can be observed more clearly and the C, Co and O elements are distributed uniformly in the nanobox. As verified by thermogravimetric analysis (TGA; Figure S13), the weight content of Co_3O_4 in the composite is about 44.5 wt%. The high-resolution XPS spectrum of Co 2p exhibits two main peaks at binding energies of 780.2 and 795.4 eV with a spin energy separation of 15.2 eV (Figure S14a), corresponding to Co 2p_{3/2} and Co 2p_{1/2} of the Co_3O_4 phase.^[35,36] The FTIR spectrum also confirms the formation of spinel Co_3O_4 (Figure S14b). Moreover, the as-prepared H- Co_3O_4 @MCNBs possess a high specific Brunauer-Emmett-Teller (BET) surface area of 392 m² g⁻¹ (Figure S15a). Notably, the distribution intensity of pore sizes is significantly increased compared to that of Co@MCNBs (Figure S10b and S15b), which should be attributed to the formation of Co_3O_4 hollow NPs. In addition, the Co_3O_4 NPs in H- Co_3O_4 @MCNBs can be completely etched by HCl to produce well-defined MCNBs (Figure S16), further revealing the favorable ion migration in the hollow porous carbon structure. The delicate integration of hollow porous carbon and well-dispersed Co_3O_4 hollow NPs is beneficial for facilitating electron conduction and Li⁺ ion migration, effectively alleviating the volume variation, as well as endowing abundant active sites for electrochemical reactions.

The electrochemical properties of the H- Co_3O_4 @MCNBs are evaluated as an anode material for LIBs. The electrochemical lithium storage behavior of the H- Co_3O_4 @MCNBs is first studied by cyclic voltammetry (CV). **Figure 4a** presents representative CV curves of the first three cycles of the electrode in a voltage window of 0.01-3.0 V (vs. Li/Li⁺). In the first cathodic scan, a broad peak at 0.64 V can be attributed to the irreversible electrochemical reduction reactions between Co_3O_4 and Li⁺, and the formation of Li₂O and solid electrolyte interphase (SEI).^[37-39] An obvious anodic peak at about 2.09 V can be assigned to the oxidation of Co NPs accompanying the decomposition of Li₂O.^[10,40] In the

subsequent cycles, the main cathodic peaks shift to 1.33 and 0.95 V, corresponding to the reduction of Co^{3+} to Co^{2+} and Co^{2+} to metal Co, respectively,^[11] suggesting the two-step reduction reactions of Co_3O_4 with Li^+ , while the anodic peaks show negligible change. The nearly identical peak intensities and integral areas reveal the good reversibility of Li^+ insertion and extraction reactions. Typical discharge-charge voltage profiles of the $\text{H-Co}_3\text{O}_4@\text{MCNBs}$ at a current density of 0.2 A g^{-1} are shown in Figure 4b. The initial discharge and charge capacities of about 1986 and 1102 mAh g^{-1} respectively can be obtained, corresponding to an initial Coulombic efficiency (CE) of about 55.5%. The initial capacity loss is mainly attributed to the possible irreversible processes (e.g., electrolyte decomposition and inevitable formation of SEI films).^[11] The nearly overlapped discharge-charge profiles of the second and third cycles further suggest the good stability and reversibility of the electrode.

Figure 4c shows the rate capability of the $\text{H-Co}_3\text{O}_4@\text{MCNBs}$ electrode cycled at various current densities. The electrode delivered reversible capacities of 1150, 1125, 984, 820 and 658 mAh g^{-1} at current densities of 0.1, 0.2, 0.5, 1 and 2 A g^{-1} , respectively. Even at a relatively high current density of 5 A g^{-1} , a remarkable capacity of 420 mAh g^{-1} can still be delivered. When the current density is abruptly returned from 5 to 0.1 A g^{-1} , the high capacity is recovered quickly in a few cycles, suggesting the excellent reversibility for lithium storage. The outstanding rate capability of the $\text{H-Co}_3\text{O}_4@\text{MCNBs}$ electrode can be further confirmed by the discharge-charge voltage curves at different current densities (Figure 4d). Moreover, the $\text{H-Co}_3\text{O}_4@\text{MCNBs}$ electrode also exhibits superior cycling stability. As shown in Figure 4e, the $\text{H-Co}_3\text{O}_4@\text{MCNBs}$ electrode shows a high capacity of 1120 mAh g^{-1} over 100 cycles with close to 100% CE at 0.2 A g^{-1} , which is superior to some of the reported Co_3O_4 -based electrodes (Table S1). Furthermore, even at a much higher current density of 1 A g^{-1} , the electrode still shows very good stability over 300 discharge-charge cycles with an average capacity fading of only 0.07% per cycle (Figure S17). Interestingly, the well-defined MCNBs can also deliver a reversible capacity of

about 850 mAh g⁻¹ over 100 cycles at 0.2 A g⁻¹ (Figure S18), contributing about 42% to the overall capacity of H-Co₃O₄@MCNBs. For comparison, hollow Co₃O₄ NPs assembled nanoboxes (H-Co₃O₄ NBs) are prepared through annealing the H-Co₃O₄@MCNBs at 300°C in air. The H-Co₃O₄ NBs exhibit a specific BET surface area of 54.9 m² g⁻¹ and similar electrochemical lithium storage behavior as H-Co₃O₄@MCNBs (Figure S19-21). As expected, the capacity of H-Co₃O₄ NBs without the confinement of mesoporous carbon fades rapidly with cycling (Figure S22). Moreover, the hollow structure of H-Co₃O₄@MCNBs is still well maintained while the H-Co₃O₄ NBs are completely pulverized after prolonged cycling (Figure S23), indicating that the nanobox structure with the carbon confinement can more effectively buffer the mechanical stress caused by the volume change during the repeated lithiation/delithiation processes. Electrochemical impedance spectroscopy (EIS) spectra show that the H-Co₃O₄@MCNBs exhibit better electrical conductivity and higher Li⁺ ion diffusion rate than H-Co₃O₄ NBs (Figure S24). Additionally, the kinetic study based on CV tests at different scan rates is performed, indicating the dominant fast kinetics of capacitance-controlled behavior in accordance with its remarkable rate performance (Figure S25).

The above results highlight the greatly enhanced lithium storage properties of the H-Co₃O₄@MCNBs, which should benefit from their distinct hollow structural and compositional features. First, the primary hollow Co₃O₄ NPs can greatly shorten the distance for fast Li⁺ ion diffusion and effectively alleviate the volume variation as well as provide sufficient active material/electrolyte contact area for the rapid charge and mass transfer, thereby achieving enhanced capacity. Second, the hollow interior in the NBs and the porosity in the wall can efficiently buffer the volume expansion and contraction upon repeated lithiation/delithiation processes and ensure fast Li⁺ ion migration. Last, the confinement of hollow Co₃O₄ NPs with high dispersion can offer very good and stable electrical contact between the active material and the electrically conducting carbon, hence resulting in the better utilization of the Co₃O₄ active

material and more interfaces for extra lithium storage.^[37] This synergistic effect between the hollow Co₃O₄ NPs and MCNBs can further improve the specific capacity and cycling stability.

In summary, we have demonstrated an elegant MOF-engaged strategy for the fabrication of highly dispersed Co₃O₄ hollow nanoparticles (sub-20 nm) embedded in the mesoporous walls of carbon nanoboxes (H-Co₃O₄@MCNBs) for efficient lithium storage. ZIF-67 NCs are used as starting material to form TA-Co NBs through a controlled chemical etching-coordination process. The as-obtained TA-Co NBs are then converted to H-Co₃O₄@MCNBs through a two-step annealing treatment. Benefiting from their unique nanostructure and composition, the H-Co₃O₄@MCNBs as a potential anode material for LIBs exhibited excellent lithium storage properties in terms of high specific capacity, superior rate capability, and long-term cycling stability. This work may inspire the design and construction of high-performance nanomaterials with novel hollow structures for various energy-related applications.

Acknowledgments

X.W.L. acknowledges the funding support from the Ministry of Education of Singapore through the Academic Research Fund (AcRF) Tier-2 grant (MOE2017-T2-2-003), and the National Research Foundation (NRF) of Singapore via the NRF Investigatorship (NRF-NRFI2016-04).

References

- [1] M. Armand, J.-M. Tarascon, *Nature* **2008**, *541*, 652.
- [2] F. Wu, J. Maier, Y. Yu, *Chem. Soc. Rev.* **2020**, *49*, 1569.
- [3] Y. Lu, L. Yu, X. W. Lou, *Chem* **2018**, *4*, 972.
- [4] S. Fang, D. Bresser, S. Passerini, *Adv. Energy Mater.* **2019**, *10*, 1902485.
- [5] Y. Lu, L. Yu, M. Wu, Y. Wang, X. W. Lou, *Adv. Mater.* **2018**, *30*, 1702875.
- [6] S. Xiong, J. S. Chen, X. W. Lou, H. C. Zeng, *Adv. Funct. Mater.* **2012**, *22*, 861.
- [7] D. Wang, Y. Yu, H. He, J. Wang, W. Zhou, H. D. Abruña, *ACS Nano* **2015**, *9*, 1775.
- [8] Y. M. Chen, L. Yu, X. W. Lou, *Angew. Chem. Int. Ed.* **2016**, *55*, 5990.

- [9] Y. Hou, J. Li, Z. Wen, S. Cui, C. Yuan, J. Chen, *Nano Energy* **2015**, *12*, 1.
- [10] J. Wang, H. Wang, F. Li, S. Xie, G. Xu, Y. She, M. K. H. Leung, T. Liu, *J. Mater. Chem. A* **2019**, *7*, 3024.
- [11] J. Zhu, W. Tu, H. Pan, H. Zhang, B. Liu, Y. Cheng, Z. Deng, H. Zhang, *ACS Nano* **2020**, *14*, 5780.
- [12] Z.-S. Wu, W. Ren, L. Wen, L. Gao, J. Zhao, Z. Chen, G. Zhou, F. Li, H.-M. Cheng, *ACS Nano* **2010**, *4*, 3187.
- [13] X. W. Lou, D. Deng, J. Y. Lee, J. Feng, L. A. Archer, *Adv. Mater.* **2008**, *20*, 258.
- [14] H. Tabassum, R. Zou, A. Mahmood, Z. Liang, Q. Wang, H. Zhang, S. Gao, C. Qu, W. Guo, S. Guo, *Adv. Mater.* **2018**, *30*, 1705441.
- [15] R. Wu, D. P. Wang, X. Rui, B. Liu, K. Zhou, A. W. Law, Q. Yan, J. Wei, Z. Chen, *Adv. Mater.* **2015**, *27*, 3038.
- [16] J. Zhang, L. Yu, X. W. Lou, *Nano Res.* **2017**, *10*, 4298.
- [17] X. W. Lou, L. A. Archer, Z. Yang, *Adv. Mater.* **2008**, *20*, 3987.
- [18] M. Fan, D. Liao, M. F. A. Aboud, I. Shakir, Y. Xu, *Angew. Chem. Int. Ed.* **2020**, *59*, 8247.
- [19] Z. Liang, R. Zhao, T. Qiu, R. Zou, Q. Xu, *EnergyChem* **2019**, *1*, 100001.
- [20] Z. X. Cai, Z. L. Wang, J. Kim, Y. Yamauchi, *Adv. Mater.* **2019**, *31*, 1804903.
- [21] H. Hu, B. Y. Guan, X. W. Lou, *Chem* **2016**, *1*, 102.
- [22] M. Hu, Y. Ju, K. Liang, T. Suma, J. Cui, F. Caruso, *Adv. Funct. Mater.* **2016**, *26*, 5827.
- [23] W. Zhang, X. Jiang, Y. Zhao, A. Carne-Sanchez, V. Malgras, J. Kim, J. H. Kim, S. Wang, J. Liu, J. S. Jiang, Y. Yamauchi, M. Hu, *Chem. Sci.* **2017**, *8*, 3538.
- [24] P. Zhang, B. Y. Guan, L. Yu, X. W. Lou, *Angew. Chem. Int. Ed.* **2017**, *56*, 7141.
- [25] H. Ejima, J. J. Richardson, K. Liang, J. P. Best, M. P. v. Koevenden, G. K. Such, J. Cui, F. Caruso, *Science* **2013**, *341*, 154.
- [26] J. Wei, Y. Liang, Y. Hu, B. Kong, J. Zhang, Q. Gu, Y. Tong, X. Wang, S. P. Jiang, H. Wang, *Angew. Chem. Int. Ed.* **2016**, *55*, 12470.
- [27] Y. Shi, Y. Yu, Y. Liang, Y. Du, B. Zhang, *Angew. Chem. Int. Ed.* **2019**, *58*, 3769.
- [28] X. Wang, Z. Na, D. Yin, C. Wang, Y. Wu, G. Huang, L. Wang, *ACS Nano* **2018**, *12*, 12238.
- [29] Y. Liang, J. Wei, Y. X. Hu, X. F. Chen, J. Zhang, X. Y. Zhang, S. P. Jiang, S. W. Tao, H. T. Wang, *Nanoscale* **2017**, *9*, 5323.
- [30] X. F. Lu, L. Yu, X. W. Lou, *Sci. Adv.* **2019**, *5*, eaav6009.

- [31] S. Wang, Y. Wang, S. L. Zhang, S. Q. Zang, X. W. Lou, *Adv. Mater.* **2019**, *31*, 1903404.
- [32] Y. Yin, R. M. Rioux, C. K. Erdonmez, S. Hughes, G. A. Somorjai, A. P. Alivisatos, *Science* **2004**, *304*, 711.
- [33] C. Guan, A. Sumboja, H. Wu, W. Ren, X. Liu, H. Zhang, Z. Liu, C. Cheng, S. J. Pennycook, J. Wang, *Adv. Mater.* **2017**, *29*, 1704117.
- [34] D. Ji, L. Fan, L. Tao, Y. Sun, M. Li, G. Yang, T. Q. Tran, S. Ramakrishna, S. Guo, *Angew. Chem. Int. Ed.* **2019**, *58*, 13840.
- [35] Y. P. Zhu, T. Y. Ma, M. Jaroniec, S. Z. Qiao, *Angew. Chem. Int. Ed.* **2017**, *56*, 1324.
- [36] H. Wang, S. Zhuo, Y. Liang, X. Han, B. Zhang, *Angew. Chem. Int. Ed.* **2016**, *55*, 9055.
- [37] Y. Dou, J. Xu, B. Ruan, Q. Liu, Y. Pan, Z. Sun, S. X. Dou, *Adv. Energy Mater.* **2016**, *6*, 1501835.
- [38] J. Y. Cheong, J. H. Chang, S.-H. Cho, J.-W. Jung, C. Kim, K. S. Dae, J. M. Yuk, I.-D. Kim, *Electrochim. Acta* **2019**, *295*, 7.
- [39] D. Wu, C. Wang, H. Wu, S. Wang, F. Wang, Z. Chen, T. Zhao, Z. Zhang, L. Y. Zhang, C. M. Li, *Carbon* **2020**, *163*, 137.
- [40] M. Yu, Y. Sun, H. Du, C. Wang, W. Li, R. Dong, H. Sun, B. Geng, *Electrochim. Acta* **2019**, *317*, 562.

Figures and Captions

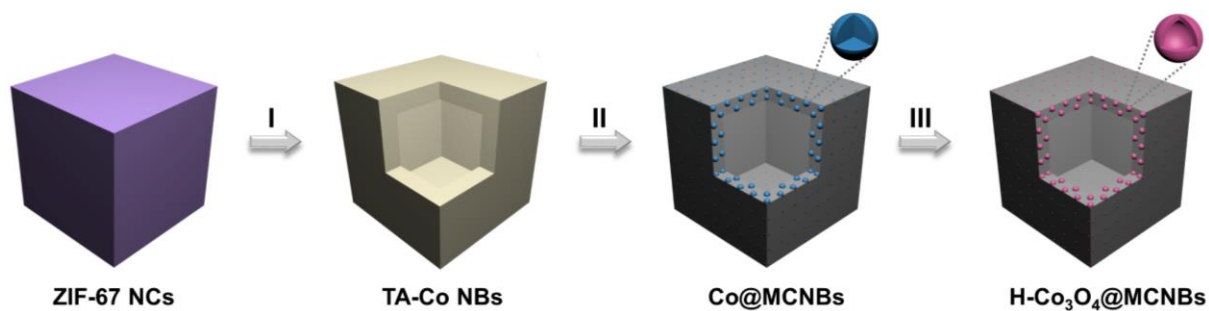


Figure 1. Schematic illustration of the formation process of H-Co₃O₄@MCNBs. Step I: Etching of ZIF-67 NCs by TA to form TA-Co NBs. Step II: Carbonization in N₂ to form Co@MCNBs. Step III: Calcination of Co@MCNBs in air to obtain H-Co₃O₄@MCNBs.

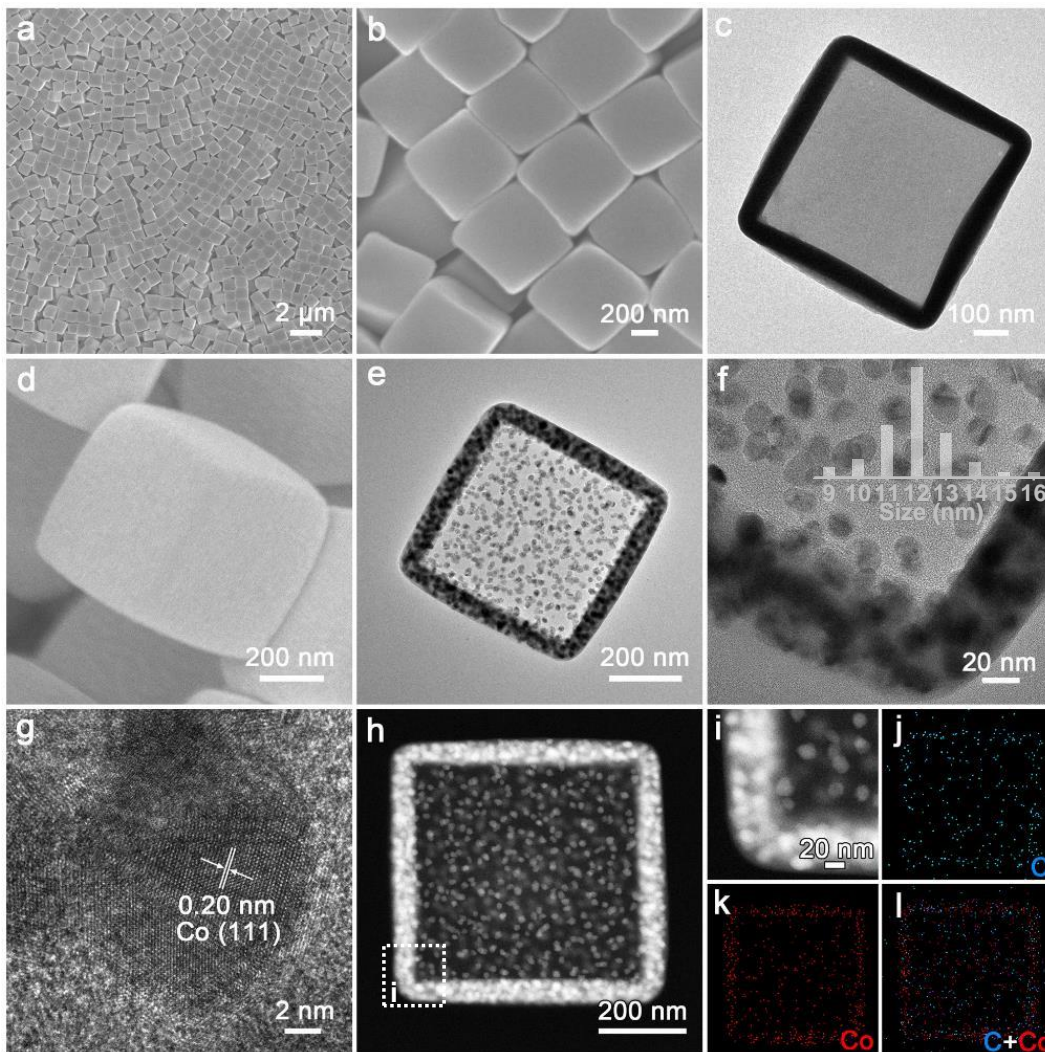


Figure 2. (a, b) FESEM, (c) TEM images of TA-Co NBs. (d) FESEM, (e, f) TEM (inset: size distribution histogram of the Co NPs), (g) HRTEM, (h, i) HAADF-STEM images of Co@MCNBs. Elemental mapping images of C (j), Co (k), overlay (l) of an individual Co@MCNB.

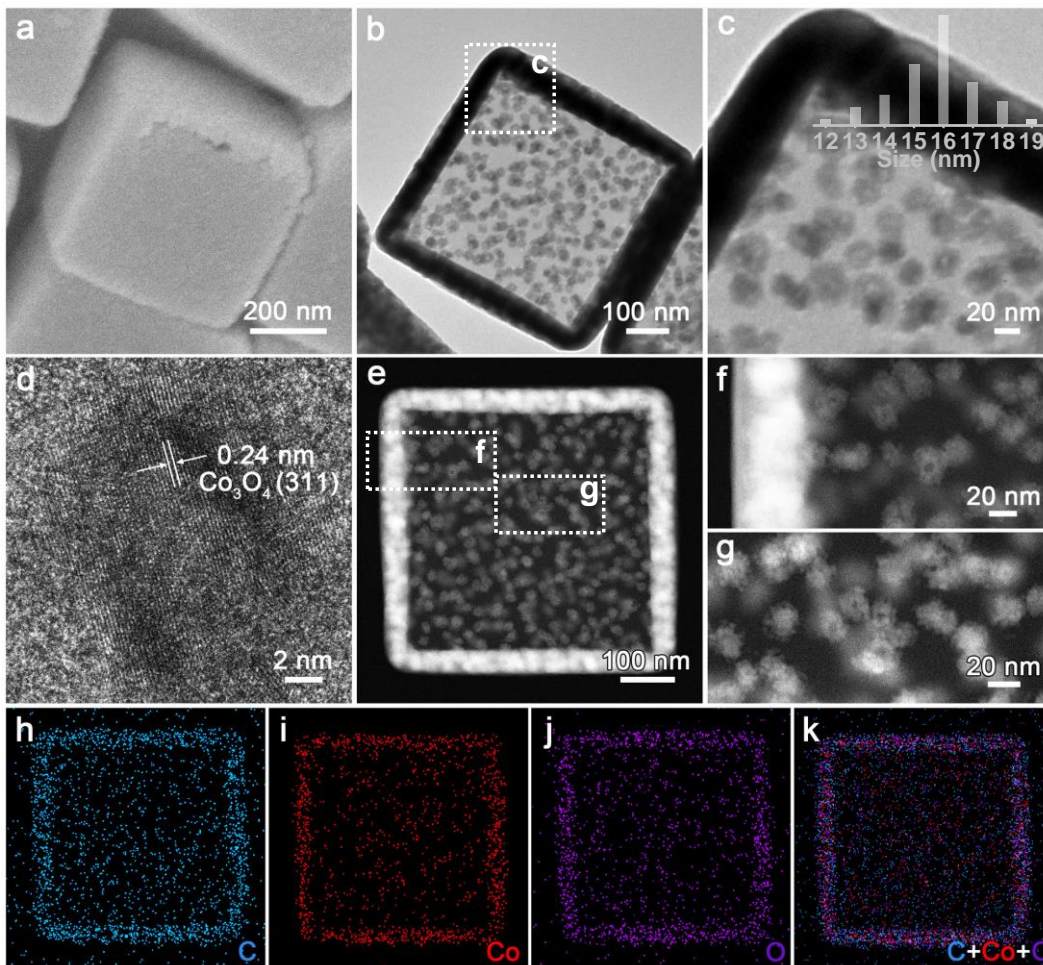


Figure 3. (a) FESEM, (b, c) TEM (inset: size distribution histogram of the Co₃O₄ hollow NPs), (d) HRTEM, (e-g) HAADF-STEM images of H-Co₃O₄@MCNBs. Elemental mapping images of C (h), Co (i), O (j) and overlay (k) of an individual H-Co₃O₄@MCNB.

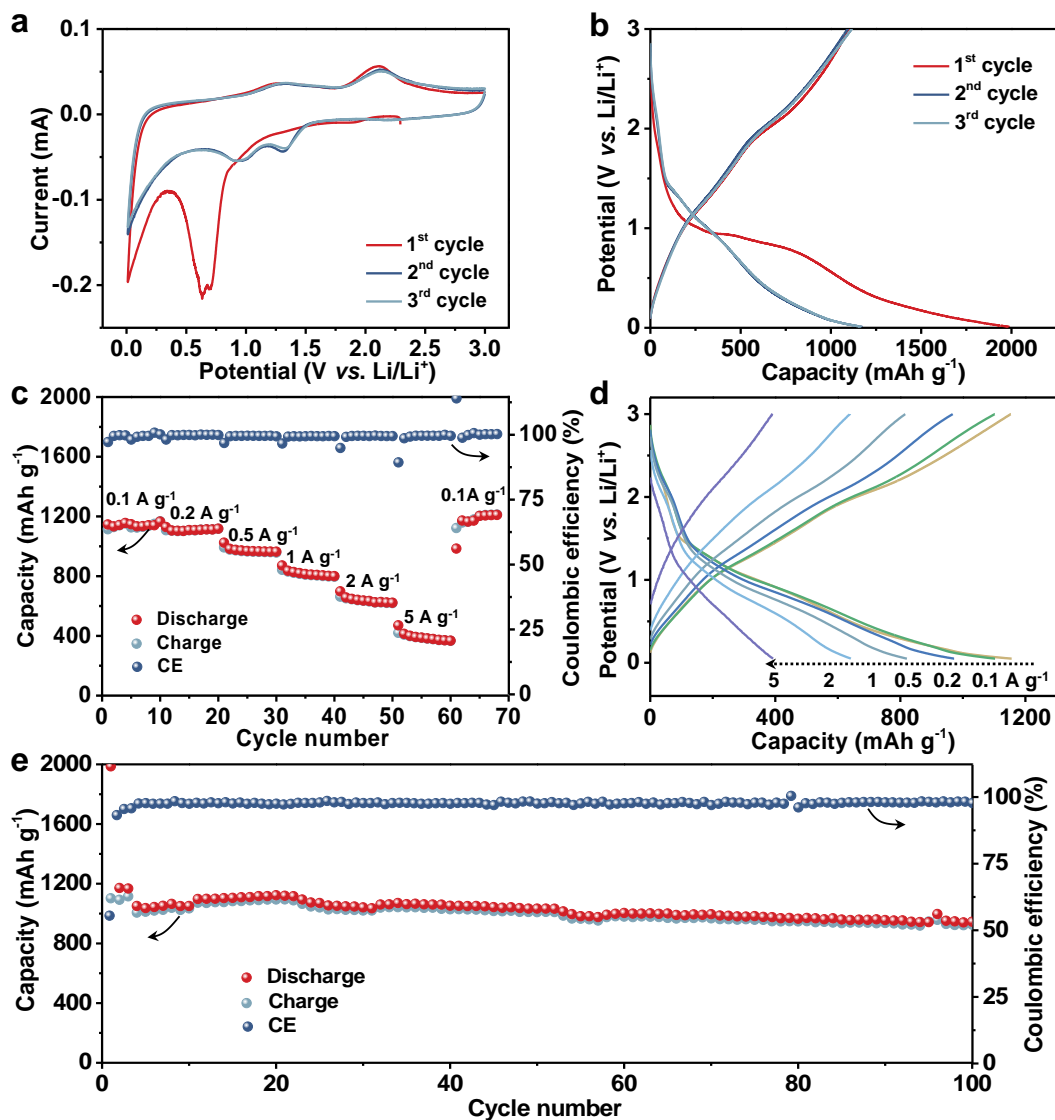
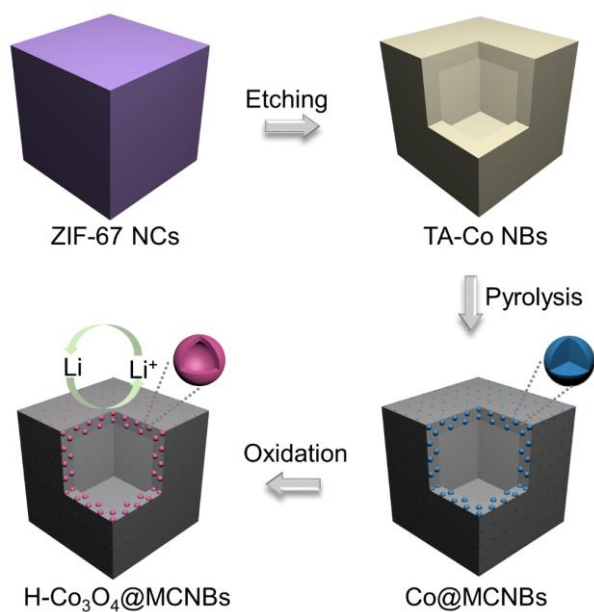


Figure 4. Electrochemical performance of H-Co₃O₄@MCNBs for lithium storage. (a) CV curves of the first three cycles at a scan rate of 0.1 mV s⁻¹. (b) Galvanostatic discharge-charge voltage profiles for the first three cycles at a current density of 0.2 A g⁻¹. (c) Rate performance and Coulombic efficiency, and (d) the corresponding discharge-charge voltage profiles at various current densities. (e) Cycling performance at a current density of 0.2 A g⁻¹ and the corresponding Coulombic efficiency.

for Table of Content Entry



Hybrid hollow architectures composed of highly dispersed Co₃O₄ hollow nanoparticles embedded in the walls of mesoporous carbon nanoboxes (H-Co₃O₄@MCNBs) are synthesized through an elaborate etching-pyrolysis-oxidation strategy starting from ZIF-67 nanocubes. Owing to the unique structural and compositional advantages, the obtained H-Co₃O₄@MCNBs exhibit excellent lithium storage properties as an anode material.